

#### 4. CONCLUSIONS

In this article, we have, for the first time to our knowledge, modeled the optical nanowaveguide coupler using a METM method. The relation of coupler input and output is expressed by a matrix equation. For the parallel region, a transportation matrix is used to describe the transportation properties of symmetric mode and antisymmetric mode. For the splitter regions, two transition matrices are used to describe the mode transition from single mode of input ports to the supermodes in parallel region and vice versa. For the slab waveguide case, the parameters of transition matrices were identified using mode expansion method theoretically. The analytical results are compared with the FDTD simulation results. Excellent agreement has been obtained between the simulation results and analytical results. For the 3D nanofiber coupler case, with the parallel nanofibers mode profiles obtained from 2D FEM method, we could have a similar matrix equation for the input and output relation. For the strongly coupling case, the profile of supermodes cannot be represented by a linear combination of the vector modes of the individual nanowaveguide, which is beyond the coupled mode theory assumption. METM could give a general description for it. We believe that the proposed model will be very useful to guide and assist the nanofiber and nanowires optical devices design.

#### REFERENCES

1. P.P. Bishnu, Fundamentals of fiber optics in telecommunication and sensor systems, Wiley, New York, 1993.
2. M. Ohtsu, K. Kobayashi, T. Kawazoe, T. Yatsui, and M. Naruse, Principles of nanophotonics, Taylor & Francis Group, LLC 2008.
3. L. Tong, R.R. Gattass, J.B. Ashcom, S. He, J. Lou, M. Shen, I. Maxwell, and E. Mazur, Subwavelength-diameter silica wires for low-loss optical wave guiding, *Nature* 426 (2003), 816–819.
4. L. Tong, J. Lou, and E. Mazur, Single-mode guiding properties of subwavelength-diameter silica and silicon wire waveguides, *Opt Express* 12 (2004), 1025–1035.
5. A. Yariv, Universal relations for coupling of optical power between microresonators and dielectric waveguides, *Electron Lett* 36 (2000), 321–322.
6. L. Caruso and I. Montrosset, Analysis of a racetrack microring resonator with MMI coupler, *J Lightwave Technol* 21 (2003), 206–210.
7. K. Huang, S. Yang, and L. Tong, Modeling of evanescent coupling between two parallel optical nanowires, *Appl Opt* 46 (2007), 1429–1434.
8. Y. Li and L. Tong, Mach-Zehnder interferometers assembled with optical microfibers or nanofibers, *Opt Lett* 33 (2008), 303–305.
9. F. Xia, L. Sekaric, and Y.A. Vlasov, Mode conversion losses in silicon-on-insulator photonic wire based racetrack resonators, *Opt Express* 19 (2006), 3872–3886.
10. X. Jiang, Y. Chen, G. Vienne, and L. Tong, All-fiber add-drop filters based on microfiber knot resonators, *Opt Lett* 32 (2007), 1710–1712.
11. B.P. Little, J.S. Foresi, G. Steinmeyer, E.R. Thoen, S.T. Chu, H.A. Haus, E.P. Ippen, L.C. Kimerling, and W. Greene, Ultra-compact Si-SiO<sub>2</sub> microring resonator optical channel dropping filters, *IEEE Photon Technol Lett* 10 (1998), 549–551.
12. S. Emelett and R. Soref, Analysis of dual-microring-resonator cross-connect switches and modulators, *Opt Express* 13 (2005), 7840–7853.
13. M. Sumetsky, Recent progress in the theory and applications of optical microfibers, *Proc SPIE* 6593 (2007), 659302–1.
14. S.J. Emelett and R. Soref, Design and simulation of silicon microring optical routing switches, *J Lightwave Technol* 23 (2005), 1800–1807.

15. J. Poon, J. Scheuer, S. Mookherjea, G.T. Paloczi, Y. Huang, and A. Yariv, Matrix analysis of microring coupled-resonator optical waveguides, *Opt Express* 12 (2004), 90–103.
16. I. Chremmos and N. Uzunoglu, Propagation in a directional coupler of parallel microring coupled-resonator optical waveguides, *Opt Commun* 281 (2008), 3381–3389.
17. J. Lou, L. Tong, and Z. Ye, Modeling of silica nanowires for optical sensing, *Opt Express* 13 (2005), 2135–2140.
18. F. Xu, V. Pruneri, V. Finazzi, and F. Brambilla, An embedded optical nanowire loop resonator refractometric sensor, *Opt Express* 16 (2008), 1062–1067.
19. W. Huang, Coupled-mode theory for optical waveguides: An overview, *Proc Soc Photo Opt Instrum Eng* 11 (1994), 963–983.
20. T.A. Ramadan, R. Scarmozzino, and R.M. Osgood, Adiabatic couplers design rules and optimization, *J Lightwave Technol* 16 (1998), 277–283.
21. H.S. Huang, H.-Chun, and Chang, Analysis of optical fiber directional coupling based on the HE<sub>11</sub> modes. I. The identical-core case, *J Lightwave Technol* 8 (1990), 823–831.
22. G. Cusmai, F. Morichetti, P. Rosotti, R. Costa, and A. Melloni, Circuit oriented modelling of ring resonators, *Opt Quantum Electron* 37 (2005), 343–358.
23. K.S. Chiang, C.H. Kwan, and K.M. Lo, Effective-index method with built-in perturbation correction for the vector modes of rectangular-core optical waveguides, *J Lightwave Technol* 17 (1999), 716–722.
24. C.H. Kwan and K.S. Chiang, Study of polarization-dependent coupling in optical waveguide directional couplers by the effective-index method with built-in perturbation correction, *J Lightwave Technol* 20 (2002), 1018–1026.
25. S.-W. Yang and H.-C. Chang, Numerical modeling of weakly fused fiber-optic polarization beamsplitters. II. The three-dimensional electromagnetic model, *J Lightwave Technol* 16 (1998), 691–696.
26. C.K. Madsen, Optical fiber design and analysis: A signal processing approach, Wiley, New York, NY, 1999.
27. K. Ogusu, Transmission characteristics of single-mode asymmetric dielectric waveguide Y-junctions, *Opt Commun* 53 (1985), 169–172.
28. T. Kato and Y. Kokubun, Three-dimensional propagation analysis of coupling efficiency using segmentation and local normal mode expansion for vertically coupled microring resonator filter, *J Lightwave Technol* 23 (2005), 2549–2554.

© 2010 Wiley Periodicals, Inc.

## INTRINSIC AND EXTRINSIC FIBER FABRY-PEROT SENSORS FOR ACOUSTIC DETECTION IN LIQUIDS

S. E. U. Lima,<sup>1</sup> O. Frazão,<sup>1</sup> R. G. Farias,<sup>2</sup> F. M. Araújo,<sup>1</sup> L. A. Ferreira,<sup>1</sup> V. Miranda,<sup>1,3</sup> and J. L. Santos<sup>1,4</sup>

<sup>1</sup>INESC Porto, Rua do Campo Alegre, 687, Porto 4169-007, Portugal; Corresponding author: ofrazao@inescporto.pt

<sup>2</sup>Faculdade de Engenharia da Computação, Universidade Federal do Pará, Belém, Brasil

<sup>3</sup>Faculdade de Engenharia da Universidade do Porto, Rua Dr. Roberto Frias, s/n, Porto 4200-465, Portugal

<sup>4</sup>Faculdade de Ciências da Universidade do Porto, Rua do Campo Alegre, 687, Porto 4169-007, Portugal

Received 22 July 2009

**ABSTRACT:** This article reports the development of two sensing head configurations based on extrinsic and intrinsic fiber Fabry-Pérot interferometers for the detection of incipient faults in oil-filled power transformers. The performances of the sensing heads are characterized and compared with the situations where it operates in air, water, and oil and promising results are obtained, which will allow the industrial

**Key words:** power transformers; partial discharges; acoustic detection;  
 optical fiber sensors; Fabry-Pérot interferometer

## 1. INTRODUCTION

Acoustic emissions (AE) in power transformers are generated by electrical sources (such as partial discharge and arcing) and by mechanical sources (such as loose clamping, bolts or insulation parts). It is possible to identify the AE source using the characteristic signature of each emission; indeed, from this signature emission parameters such as burst rate and count rate can be evaluated and compared with those derived from known AE sources [1–3].

Insulation degradation is mainly associated with the occurrence of partial discharges (PDs). These are an electrical phenomenon that occurs within a transformer whenever the voltage stress is sufficient to produce ionization within the solid dielectric, at conductor/dielectric interfaces or in bubbles within liquid dielectrics such as oil. High-frequency transient current discharges will then appear repeatedly and will progressively deteriorate the insulation, ultimately leading to breakdown [4]. In power transformers, the levels of PDs are an indicator of the insulation condition, because they result of localized electrical breakdown that should not be present in significant values in a good insulation system. Any PD activity has detrimental effects on the insulating materials (paper, polymers) surrounding the conductors and degrades the insulating properties of the oil, and thus its prognosis and diagnosis are of utmost importance [5].

The energy released in PDs produces a number of effects, resulting in chemical and structural changes and electromagnetic emissions [6]. Acoustic PD detection is based on the mechanical pressure wave emitted from the discharge. The AE of PDs has wideband frequency content (20–500 kHz), but considering the energy density, a sensor with response in the frequency range of 20–100 kHz is considered as a good acoustic PD detector [7]. In general, it is important not only to detect PD activity but also to give an indication of the PD source location. Traditional methods use piezoelectric sensors mounted on the outside of the wall of the transformer tank to achieve acoustic PD location. This method has problems with the high attenuation in the wall, as well as the issue of multiple routes between source and sensor that can diminish dramatically the accuracy of PD location [8]. This accuracy can be very much improved using optical fiber sensors that can be placed inside the transformer tank without affecting the insulation integrity.

With the intrinsic advantages of fiber optics sensors in mind, this article describes the development of two sensing heads based on: Extrinsic Fabry-Pérot Interferometer (EFPI) and Intrinsic Fabry-Pérot Interferometer (IFPI), for detection of AE in power transformers. The sensing fibers are attached to a diaphragm that vibrates in the presence of an acoustic wave. A laser was used to interrogate the sensors, and the detection scheme uses a computer-based feedback loop, in a homodyne configuration, to tune the laser wavelength emission and track the quadrature point, optimizing the measured and readout sensitivity. The sensitivity, distance, and frequency responses are experimentally obtained, and the effects in the characteristics of the sensing heads when they are immersed in fluids (air, water, and oil) are addressed. Future research paths are summarized in the Section 4.

## 2. BACKGROUND AND EXPERIMENTAL

Acoustic sensing has been one of the first successful applications of fiber optic sensors, and the literature on optical fiber interferometry for acoustic and ultrasonic sensing is extensive. Underwater acoustic sensing has been studied since the end of the 1970s, and many configurations were proposed to optimize system performance [9–11]. This application is well suited for interferometric sensors because the sensitivity of such sensors is high and scalable by selection of the sensing fiber length. Furthermore, acoustic sensing does not require DC sensitivity, which is the domain where interferometric sensors are not attractive because of their inherent susceptibility to signal drift (in the limit, imposed by temperature fluctuations). Michelson, Mach-Zehnder, and Sagnac interferometric configurations were used in successful designs of acoustic sensors [12–16]. However, a common problem with these sensors is the requirement for long sensing lengths to achieve sufficient acoustic sensitivity. To avoid this constrain and looking for applications in AE detection in power transformers environments, we have developed an optical sensing head based on extrinsic and intrinsic Fabry-Pérot Cavities (FPC).

### 2.1. Diaphragm Vibration—Mathematical Description

The vibration model of a circular plate is well known [17, 18]. The exact solution of this vibration problem involves the use of Bessel functions. The vibration model of a thin plate can be used to select the dimensional parameters (radius and thickness) of the diaphragm and the characteristics of its material (Young modulus and Poisson ratio), to maximize the sensor sensitivity and to satisfy some requirements (e.g., maximum static pressure operation, directionality, and frequency response). Equation (1) describes the displacement  $d$  for the central point of a diaphragm (the out-of-plane deflection) in terms of the pressure wave frequency  $f$  and the order of the excited vibration mode  $(m,n)$ ,

$$d(f) = \Delta \sum_{m=0}^{\infty} \sum_{n=0}^{\infty} \left[ \frac{A_{mn} \omega_{mn}^2}{\sqrt{(\omega_{mn}^2 - 4\pi^2 f^2)^2 + 16\pi^2 f^2 n^2}} \right] \quad (1)$$

with,

$$\Delta = \frac{3P(1 - \nu^2)}{16Et^3} a^4, \quad (2)$$

where  $\nu$  is the Poisson's ratio,  $E$  is the Young's modulus,  $t$  is the plate thickness,  $a$  its radius,  $P$  is the pressure wave amplitude,  $n$  and  $m$  are modal numbers, and  $\omega_{mn}$  is the natural frequency of the  $(m,n)$  vibration mode.

The resonance frequencies are given by

$$\omega_{m,n} = \frac{(\lambda a)_{mn}^2}{a^2} \sqrt{\frac{Et^2}{12\rho(1 - \nu^2)}} \quad (3)$$

where  $\rho$  is the mass density and  $(\lambda a)_{mn}$  are the roots of the vibration equation. Their values for some  $(m,n)$  combinations are given in Table 1.

If a diaphragm is immersed in a fluid, the resonance frequencies will be lower because of the added mass effect and it will also change the amplitude at the peak because of reradiation of acoustic energy. The new values of the natural frequencies can be calculated by

**TABLE 1** Values for  $(\lambda a)_{mn}$

$m$	$N$			
	0	1	2	3
0	3.196	4.611	5.906	7.143
1	6.306	7.799	9.197	10.537
2	9.440	10.958	12.402	13.795
3	12.577	14.108	15.579	17.005

$$\omega'_{m,n} = \frac{1}{\sqrt{1+\zeta}} \omega_{m,n} \quad (4)$$

with

$$\zeta = 0.6689 \frac{\rho_l a}{\rho t}, \quad (5)$$

where  $(\rho_l/\rho)$  is the ratio of the fluid density to the material density of the diaphragm.

### 2.2. EFPI Sensor Configuration

The EFPI sensor configuration is shown in Figure 1. The transducer element is a diaphragm that vibrates in the presence of an acoustic wave. The optical part of the sensing head consists of a lead-in/lead-out monomode fiber that is aligned with a reflecting fiber (multimode) inside a hollow glass capillary tube. With this arrangement, an extrinsic FPC is formed between the two fiber ends. The light from a laser source propagates along a lead-in monomode fiber to the FPC, which is formed by the lead-in/-out and target fibers. A fraction of  $\sim 4\%$  of this incident light is reflected at the output end face of the lead-in/-out fiber and returns directly back down the fiber. The light transmitted out of the lead-in/-out fiber is projected onto the fiber end face of the target fiber. The reflected light from the target fiber is partially recoupled into the lead-in/-out fiber. Then, the interference between the two reflections gives rise to the interfering fringes. Figure 2 shows the corresponding interferometric channeled spectrum of this structure. This interferometric spectrum is changed by the cavity length. Thus, the sensor operation is based on the transduction of the diaphragm vibration, in the presence of an acoustic wave, into a cavity length variation.

### 2.3. IFPI Sensor Configuration

In this sensor configuration, an intrinsic FPC was formed between a FBG reflector and a mirrored end surface of the fiber. To obtain a high visibility (97%), it was used a FBG with 40% of reflectivity, as the first reflection mirror, and the second reflection occurs in the silver end glass surface of the fiber, with 98% of reflectivity. Figure 3 shows the interferometric chan-

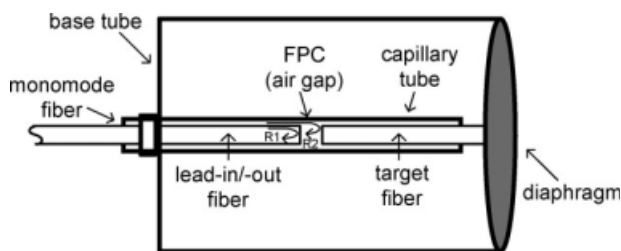


**Figure 1** The EFPI sensor configuration

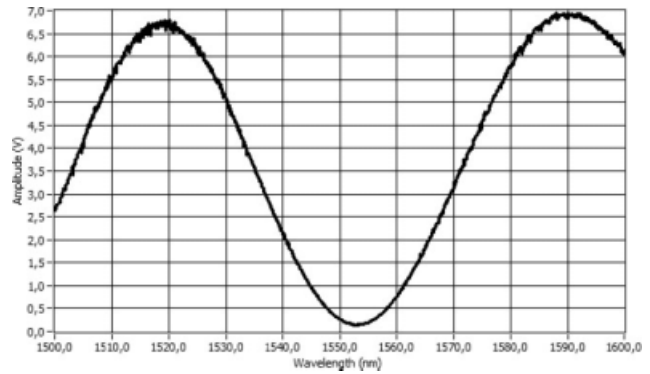


**Figure 2** Channeled spectrum of the EFPI sensor configuration

neled spectrum of the obtained structure. This pattern is characterized by a superposition of a slowly varying envelope associated with the FBG reflection spectrum and an interference fringe pattern relative to the Fabry-Perot interferometer.

The silver-mirror end-surface of the fiber is attached to a diaphragm for acoustic pressure interaction, whereas the other side of the FPC is fixed to a base cylinder (Fig. 4). The sensor operation is based on the transduction of the diaphragm vibration into fiber longitudinal strain in the presence of an acoustic wave. This pressure wave induces changes in the grating spectrum (Bragg wavelength shift) and in the interference fringe pattern (cavity length variation) simultaneously. The dynamic strain signal induces a variation of the cavity length that modulates the round-trip propagation phase shift in the Fabry-Perot interferometer. The interrogation system detects the optical power modulation induced by the relative shift of the central fringe (the one with maximum amplitude) in respect to the laser emission wavelength. Considering that the FBG spectral envelope and the interferometric fringes move synchronously under the action of the acoustic wave, there is no amplitude modulation of the central fringe associated with the spectral displacement of the envelope.

### 2.4. Interrogation System

The interrogation system (Fig. 5) is based on a tunable laser, and an active homodyne detection scheme was used to implement a high sensitivity-point tracker (operating the system in the quasi-linear region of the interference fringe spectrum). A feedback loop receives the photodetector output signal by an acquisition board and controls the wavelength of the laser emission to compensate the low-frequency variations of the photodetector signal (drift information) induced by, for example, temperature

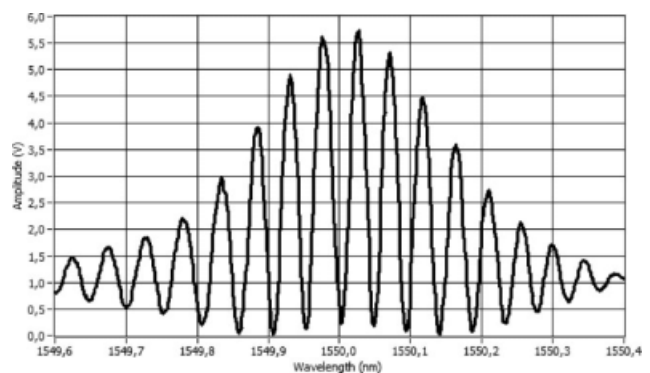


**Figure 3** Channeled spectrum of the IFPI sensor configuration

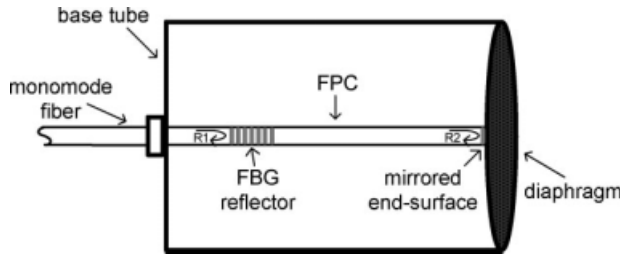


**Figure 4** The IFPI sensor configuration

changes. The detection system is locked at the highest sensitivity point (quadrature point), and any higher frequency signal is recovered directly from the photodetector output (low-bandwidth operation). LabVIEW<sup>®</sup> software was used to perform the control process and to further process the signals. The stored data is a fast Fourier transform (FFT) of the time domain photodetector electrical signal. Figure 6 shows the FFT spectrum of the sensor output signal when the piezoelectric transducer (PZT) is used to produce a 36-kHz acoustic wave in an underwater test (the PZT was 10 cm away from the sensing head). We can see the signal at 36 kHz (55 dB above the noise floor) and a harmonic at frequency of 72 kHz (30 dB above the noise floor).

### 3. RESULTS

In the experimental setup, a PZT (200LM450-ProWave) was used as an acoustic source to simulate the pressure wave from a PD. In underwater applications, the PZT has a transmitting sound pressure level of 155 dB (at 0 dB = 1  $\mu\text{Pa}/V_{\text{RMS}}$ ) with a center frequency of 200 kHz. At first, the correct operation of the detection system to compensate the temperature variations and maintain the interferometer locked at a quadrature point was verified. Thus, tests were done to evaluate the sensors response in distance and frequency.

#### 3.1. Distance Signal Dependence

The dependence with distance of the sensors response was investigated for the extrinsic and intrinsic configurations. To evaluate the sensor performance in a situation close to the one present in power transformers, the sensing head was immersed in water and in oil. The distance attenuation of the sensors output shows a similar behavior in all tests. The results for air and liquid immersed show a stronger signal in water and in oil if compared with acoustic propagation in air, and a smaller rate of the signal attenuation with distance, which are both positive features. These results are a consequence of the better acoustic energy transfer in a medium of higher density. Figures 7 and 8 show, respectively, the signal distance dependence of the EFPI and IFPI sensors.

The results of the oil-immersed tests are particularly important to evaluate the sensors performance. The results for the

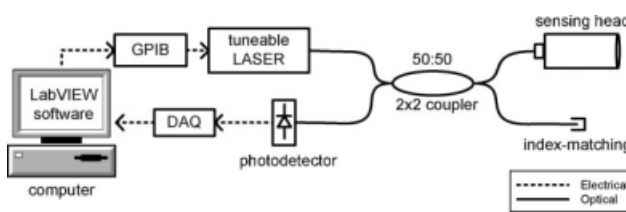


**Figure 5** Signal demodulation with active phase tracking computer-based homodyne technique

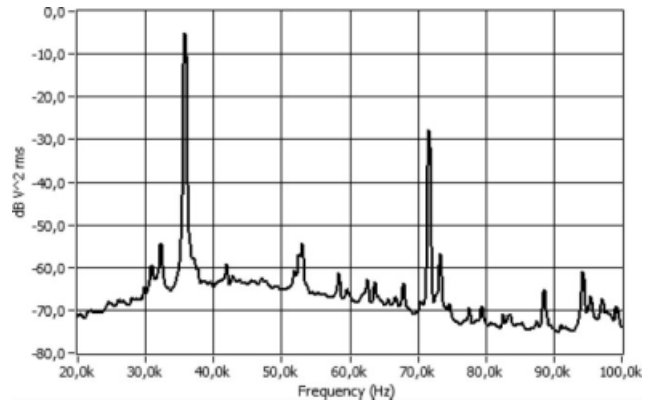


**Figure 6** FFT of the output signal of the EFPI sensor to an acoustic wave at a frequency of 36 kHz in water

EFPI sensor show a signal amplitude attenuation of 20, 15, and 12 dB for air, water, and oil-immersed cases, at a distance of 60 cm. For the IFPI sensor, the results show signal amplitude attenuation of 23, 16, and 14 dB for air, water, and oil-immersed cases, at the same distance. Thus, it turns out that the IFPI has stronger amplitude attenuation with the distance.

#### 3.2. Frequency Response

The sensor frequency response is independent of the optical sensing structure (extrinsic or intrinsic). Its characteristic depends basically on diaphragm material (Young modulus and Poisson ratio) and its geometry (radius and thickness). The frequency spectrum was obtained experimentally using a signal generator to drive the PZT. Figure 9 shows the sensor response when the frequency is swept from 1 to 100 kHz. The sweep function needs 2 min to cover the frequency range, and the experiment was carried during 20 min. Thus, the values in Figure 9 are a mean of 10 stored response values for each frequency. This experiment procedure explains the low smoothness of the response curve.

It can be observed a complex structure, certainly due to multiple resonances of the structure within this frequency window (Fig. 10). The mathematical model of the diaphragm vibration was used to simulate the dynamic behavior of the diaphragm to compare with the experimental data. The diaphragm frequency

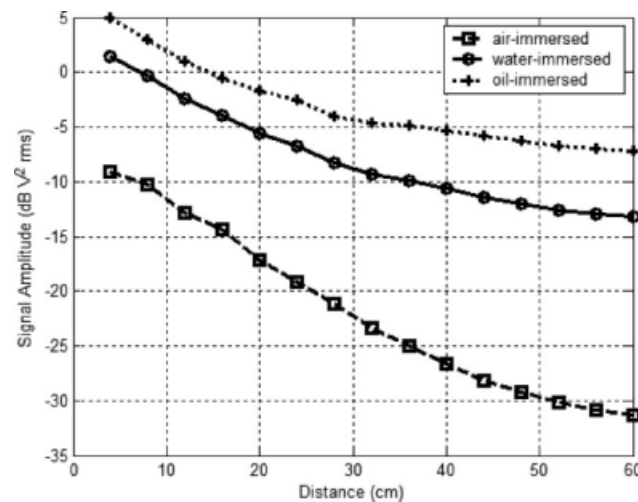


**Figure 7** The distance signal attenuation for the EFPI sensor (air, water, and oil)

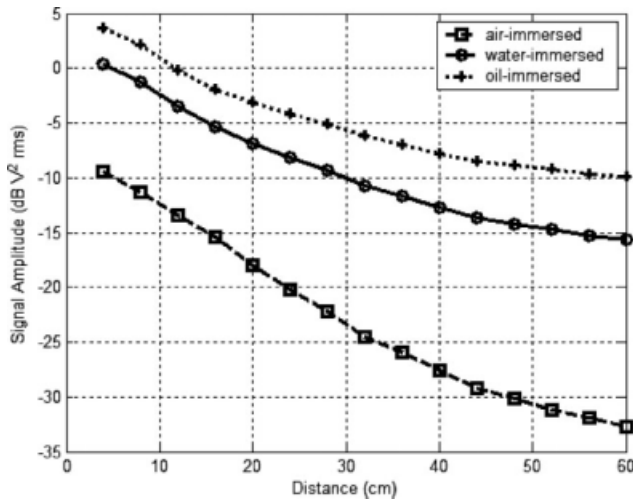


**Figure 8** The distance signal attenuation for the IFPI sensor (air, water, and oil)

response was calculated using Eq. (1) with  $n = 0$  to 3,  $m = 0$  to 3 in the frequency range (0–100) kHz. The simulated vibration behavior is close to that obtained in experimental tests (the model results are normalized). It was found that the vibration model agrees with the experimental data of water and oil immersed tests (using the correction factor given by Eq. (4) to calculate the natural frequencies in liquids).

### 3.3. Sensors Resolution

The sensors resolution have ripple amounts of about 30 dB in the frequency range (0–100) kHz and, as expected, the best resolution is obtained when some parameters of the sensor are optimized to improve responsivity at the natural vibration frequencies of the diaphragm.

The demodulation system has a  $V_{\text{RMS-noise}} = 0.5$  mV, and the PZT has a sound emitted pressure level of 105 Pa at 30 kHz. Tests are done at a distance of 10 cm (the standard distance for characterization of the acoustic emitter).

The worst acoustic receiving sensitivity for the EFPI sensor is  $-238$  dB (at  $0 \text{ dB} = 1 V_{\text{RMS}}/\mu\text{Pa}$ ) at frequency of 60 kHz, which allows a pressure resolution level of 397 Pa. At the same conditions (60 kHz, 10 cm away and  $V_{\text{RMS-noise}} = 0.5$  mV), the IFPI sensor presents a resolution level of  $-246$  dB, which

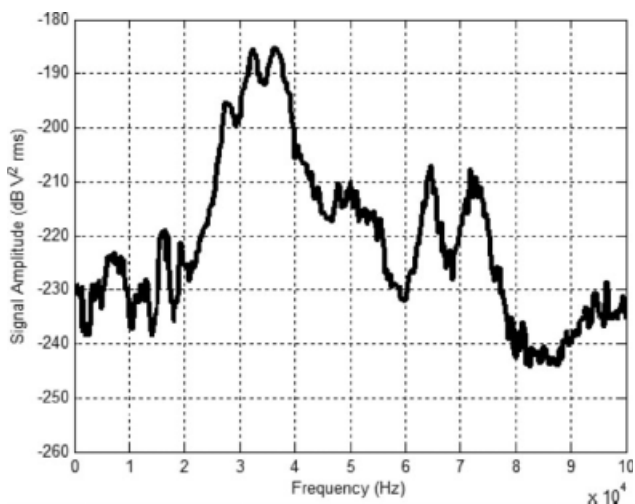


**Figure 9** Frequency response with the EFPI sensor immersed in oil

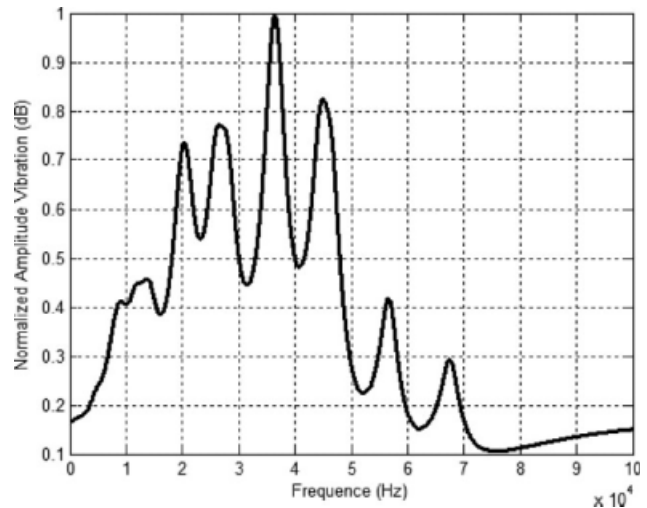


**Figure 10** Frequency response (simulated data using the plate vibration model)

allows a pressure resolution level of 998 Pa. Thus, the EFPI sensor configuration has a better pressure resolution, at the same conditions, if compared with the IFPI sensor configuration.

## 4. CONCLUSIONS

In this work, two sensing head configurations based on Extrinsic and Intrinsic Fabry-Perot Interferometers were investigated for the purpose of detecting the weak pressure wave from a PD occurrence in power transformers. The two sensing structures were attached to the same diaphragm and all sensors were interrogated by an active homodyne scheme with a tunable laser. We can conclude that the EFPI configuration has the best performance. Globally, the results obtained are promising, confirming that PD detection and measurement in power transformers are feasible using acoustic detection by sensor systems immersed in the oil, as an alternative to measurements taken from the exterior of the machine.

Further work is in progress to reach a stage where the application of these sensors in power transformers becomes feasible. In particular, the process and the materials for sensing head fabrication are being appropriately selected to support some harsh conditions (e.g., corrosive environment, high temperature, high static pressure) aiming to improve the achievable readout resolutions as well as to flatten the frequency response of the optical fiber acoustic wave transducers.

This development, which hopefully will lead to not too expensive technological solutions, also opens a new path for condition monitoring and incipient fault analysis: the placement of a number of sensors inside the transformer tank will allow the construction of three-dimensional acoustic images that will provide the pinpointing of sources of noise and eventually lead to more accurate diagnosis.

## ACKNOWLEDGMENT

Sanderson Lima acknowledges the support of Alban Programme (PhD fellowship E05D054697BR).

## REFERENCES

1. IEEE Standard C57.127-2007, Guide for the detection and location of acoustic emissions from partial discharges in oil-immersed power transformers and reactors, New York, 2007.

2. L. Lundgaard, Partial discharge, Part XIV: Acoustic partial discharge detection—Practical application, *IEEE Electr Insulation Mag* 8 (1992), 34–43.
3. P. Eleftherion, Partial discharge. XXI. Acoustic emission-based PD source location in transformers, *IEEE Electr Insulation Mag* 11 (1995), 22–26.
4. R. Bartnikas, Partial discharges: Their mechanism, detection and measurement, *IEEE Trans Dielectr Electr Insulation* 9 (2002), 763–808.
5. T. Bengtsson and B. Jönsson, Transformer PD diagnosis using acoustic emission technique, 10th International Symposium on High Voltage Engineering, Montreal, Canada, Paper no. 115, 1997.
6. V. Miranda and A.R.G. Castro, Improving the IEC table for transformer failure diagnosis with knowledge extraction from neural networks, *IEEE Trans Power Delivery* 20 (2005), 2509–2516.
7. T. Bengtsson, M. Leijon, and L. Ming, Acoustic frequencies emitted by partial discharges in oil, 8th International Symposium on High Voltage Engineering, Yokohama, Japan, Paper no. 63.10, 1993.
8. S.N. Hettiwatte, Z.D. Wang, and P.A. Crossley, Investigation of propagation of partial discharges in power transformers and techniques for locating the discharge, *IEE Proc Sci Meas Technol* 152 (2005), 25–30.
9. J.H. Cole, R.L. Johnson, and P.G. Bhuta, Fiber-optic detection of sound, *J Acoust Soc Am* 62 (1977), 1136–1138.
10. J.A. Bucaro and T.R. Hickman, Measurement of sensitivity of optical fibers for acoustic detection, *Appl Opt* 18 (1979), 938–940.
11. R.O. Claus and J.H. Cantrell, Detection of ultrasonic waves in solids by an optical fiber interferometer, *Proceedings of 1980 Ultrasonics Symposium*, IEEE, New York, 1980, pp. 849–852.
12. G.A. Cranch, P.J. Nash, and C.K. Kirkendall, Large-scale remotely interrogated arrays of fiber-optic interferometric sensors for underwater acoustic applications, *IEEE Sens J* 3 (2003), 19–30.
13. S. Atique, D. Betz, B. Culshaw, F. Dong, H.S. Park, G. Thursby, and B. Sorazu, Detecting ultrasound using optical fibres, *J Opt* 33 (2004), 231–238.
14. W. Lin, C.F. Chang, C.W. Wu, and M.C. Chen, The configuration analysis of fibre optic interferometer of hydrophones, *MTTS/IEEE TECHNO-OCEAN '04* 2 (2004), 589–592.
15. E. Udd, Fiber-optic acoustic sensor based on the Sagnac interferometer, *Proc SPIE* 425 (1983), 90–95.
16. J. Xu, X. Wang, K. Cooper, and A. Wang, Miniature all-silica fibre optic pressure and acoustic sensor, *Opt Lett* 30 (2005), 3269–3271.
17. T. Krauthammer and E. Ventsel, *Thin plates and shells: Theory, analysis and applications*, MerceL Dekker Inc., New York, 2001.
18. W. Soedel, *Vibrations of shells and plates*, 3rd ed., MerceL Dekker Inc., New York, 2004, pp. 102–106.

© 2010 Wiley Periodicals, Inc.

## A COMPACT AND LOW-LOSS LTCC DIPLEXER WITH HIGH-BAND SELECTIVITY AND HIGH ISOLATION FOR DUAL-BAND APPLICATIONS

Tae Wan Kim and Young Chul Lee

Division of Marine Electronics and Communication Engineering, Mokpo National Maritime University (MMU), 571 Chuukyo-dong, Mokpo, Jeonnam, Korea; Corresponding author: leeyc@mmu.ac.kr

Received 22 July 2009

**ABSTRACT:** This article presents a compact and low-loss diplexer for dual-band applications using a LTCC (low temperature co-fired ceramic) multilayer technology. This diplexer is composed of the high-pass filter (HPF) and low-pass filter (LPF) in order to separate GSM (global system for mobile) and CDMA (code division multiple access) band. For enhancing band selectivity of the diplexer, a shunt capacitor and inductor are designed in the HPF and LPF, respectively.

In addition, a transmission zero is designed at the stopband of the LPF using a shunt inductor for improving isolation characteristics. The diplexer is realized in a 6-layer LTCC substrate with a relative dielectric constant of 7. The size of the fabricated diplexer including CPW pads is  $3.45 \times 4.0 \times 0.7 \text{ mm}^3$ . A measured insertion loss (IL) and return loss (RL) of the GSM band are less than  $-0.54 \text{ dB}$  and  $-10.50 \text{ dB}$ , respectively. In the case of CDMA band, the IL of  $-1.13 \text{ dB}$  and RL of below  $-6.16 \text{ dB}$  are archived. © 2010 Wiley Periodicals, Inc. *Microwave Opt Technol Lett* 52: 1134–1137, 2010; Published online in Wiley InterScience (www.interscience.wiley.com). DOI 10.1002/mop.25137

**Key words:** LTCC; diplexer; multi-band; low-pass filter; high-pass filter

### 1. INTRODUCTION

Recently, a significant growth of wireless communication market is observed. A GSM (global system for mobile) and CDMA (code division multiple access) are one of the representative mobile services in the world. GSM and CDMA have been allocated 880–1900 MHz and 450–1900 MHz around world, respectively. To enable “seamless roaming” in the world, multi-band front-end modules (Mb-FEM) or transceiver modules have been researched and developed by several institutes [1–3]. In these modules, a key device is a diplexer or duplexer.

Various results [4–8] reflecting above trends have been reported for high performance and compact diplexer modules using LTCC multilayer technology, which is an attractive technology for wireless communication system-on-package (SoP) architecture because it offers a low-loss and high-integration capability [9]. To improve isolation characteristics, transmission zeros have been designed in the passband of the LTCC diplexer [4, 5]. However, transmission line structures of the diplexer resulted in a bulky module [4]. A method to minimize interferences among the embedded inductors and capacitors was proposed by avoiding the overlapped area of these passive elements [6]. However, additional BPFs were designed for improving band selection. The LTCC diplexer based on a dual BPF was reported [8] for 2.4 and 5 GHz WLAN applications. However, for reduction of its planar size, it was fabricated in a 14-layer LTCC dielectric substrate.

In this article, a compact and low-loss diplexer for dual-band (GSM and CDMA) applications is presented by using LTCC technology. To improve band selectivity and isolation characteristics, lumped elements in the low-pass filter (LPF) and high-pass filter (HPF) and a transmission zero in the LPF are designed. The designed diplexer was implemented using a 6-layer LTCC dielectric. The overall size of the fabricated diplexer including CPW pads is  $3.45 \times 4.0 \times 0.7 \text{ mm}^3$ .

### 2. DIPLEXER DESIGN

In general, Mb-FEM consist of several transceivers (TRx), switch devices, and diplexers (duplexers) [10, 11]. However, these Mb-FEM have suffered from high-power consumption, high cost, and bulky size. Therefore, using an alternative technology such as reconfigurable RF [12, 13], a compact, low-power, and intelligent Mb-FEM have been researched. To make up for the imperfect selectivity of the reconfigurable filters, even in the novel Mb-FEM, the compact and high-performance diplexer having selectivity is also required. In this work, a compact and low-loss diplexer to separate GSM from CDMA band has been designed using a LTCC technology.

#### 2.1. Schematic Circuit Design for Diplexer

Figure 1 shows a fundamental diplexer designed by using a third-order Chebyshev low-pass and HPF. Figure 2(b) illustrates